NAVIER-STOKES CALCULATION OF TURBINE FLOWS WITH FILM COOLING

ICAS-94-2.5.3

by

D.T. Vogel
Research engineer, Inst. f. Propulsion
DLR, Linder Höhe, D-51147 Köln

1 Abstract

A Navier-Stokes flow solver system consisting of a two- and threedimensional solver has been developed to simulate turbine flows with film and convective cooling. The system works on patched structured computational grids in multi block manner. The numerical method of finite volumes with central difference approximation is applied to solve the discretized Reynolds-averaged Navier-Stokes equations in a blade-attached cylindrical or cartesian frame. The low Reynolds $k-\epsilon$ model in an implicit or explicit form is used to model turbulence. Several boundary conditions can be specified on every particular piecewise defined block face allowing a great flexibility in simulating flows in very complex geometries, i.e. film cooling from rows of holes. As demonstrated in Fig. 4 film cooling in flow regions with strong gradients, i.e. stagnation points, the discretization of the whole film cooling geometry is necessary to obtain accurate solutions. The flow solver is able to calculate turbine film cooling with simultanous solution of the "outer" turbine and the "inner" cooling system flow. The system is vectorized for the use on super-vector computers only using 1D loops and parallized using message passing on parallel computers.
The validation of the system with experimental test data show good agreement.

2 List of symbols

n	Normal vector
λ	thermal conductivity
μ	viscosity
V	velocity
H	Total enthalpy
D	Dissipation
Ω	rotational speed
ω	Rotation vector
Γ	Surface normal vector
x, y, z	cartesian coordinates
RES	Residual

Subscripts

n	normal direction
x, y, z	in direction of cartesian coordiantes
rot	Rotation
farfi	Farfield
extr	Extrapolated form th flow field

3 The Navier-Stokes Solver

3.1 Physical model and governing equations

The governing equations (Reynolds–averaged Navier–Stokes, continuity and energy equations, Eq. 1) are numerically solved using a finite volume technique with a cell centred difference approximation of second order accuracy to represent the convection and diffusion terms in space and a second order time-accurate explicit three or five step Runge-Kutta algorithm for the time discretization. More stability is gained by using a residual averaging method which can be run either implicit, or if the user wishes, explicit. The maximal timesteps which lead to a steady solution are calculated from the CFL-criteria. Eigenvalue-scaled scalar artificial dissipation with operators of second and fourth order is added to the numerical scheme to damp out non-physical wiggles produced by the central differencing scheme and to capture physical discontinuities as shocks and strong free shear layers. Eq. 4 demonstrates the artificial dissipation model with scalar-eigenvalue-scaling introduced by Swanson and Turkel ([8], 1987). For multidimensional subsonic and transonic complex flows with strong physical viscous damping this scheme supplies acceptable solutions. The rotational fluxes occuring in rotor flows (Eq. 1) are solved in conservation form ([4], [5]).
The governing equations are written as:

$$\frac{\partial \vec{Q}}{\partial t} + \frac{\partial \vec{F_1}}{\partial x} + \frac{\partial \vec{F_2}}{\partial y} + \frac{\partial \vec{F_3}}{\partial z} = \frac{\partial \vec{F_{v1}}}{\partial x} + \frac{\partial \vec{F_{v2}}}{\partial y} + \frac{\partial \vec{F_{v3}}}{\partial z} + \vec{G_{rot}} \tag{1}$$

with $\vec{Q} = (\rho, \rho u, \rho v, \rho w, \rho E_{rot})^T$ the vector of the conservative variables and the convective and diffusive fluxes:

$$\begin{aligned} F_1 &= (\rho u, \rho uu + p, \rho vu, \rho wu, \rho H_{rot} u)^T \\ F_2 &= (\rho(v - v_r), \rho u(v - v_r, \rho v(v - v_r) + p, \\ &\quad \rho w(v - v_r), \rho H_{rot}(v - v_r))^T \\ F_3 &= (\rho(w - w_r), \rho u(w - w_r), \rho v(w - w_r), \\ &\quad \rho(w - w_r)w + p, \rho H_{rot}(w - w_r))^T \end{aligned}$$

$$F_{v1} = (0, \tau_{xx}, \tau_{yx}, \tau_{zx}, D_{v_x})^T$$
$$F_{v2} = (0, \tau_{xy}, \tau_{yy}, \tau_{zy}, D_{v_y})^T$$

$F_{v3} = (0, \tau_{xz}, \tau_{yz}, \tau_{zz}, D_{v_z})^T$

and the source vector:
$\vec{G_{rot}} = (0, 0, \rho\Omega w, -\rho\Omega v, 0)^T$

The static pressure can be expressed with the help of the law of the ideal gas:

$$p = (\kappa - 1)(\rho E_{rot} + \rho(\vec{V}(\vec{\omega} \times \vec{r}) - \frac{1}{2}\vec{V}\vec{V}))$$

and $H_{rot} = E_{rot} + \frac{p}{\rho}$
The product of $\vec{V}(\vec{\omega} \times \vec{r})$ supplies:

$$\vec{V}(\vec{\omega} \times \vec{r}) = \Omega(yw - zv)$$

and the vector of the rotational speed is read as:

$$(u_r, v_r, w_r)^T = \Omega(0, -z, y)^T$$

The use of a curvilinear coordinate system (ξ, η, ζ) requires a transformation with the Jacobian (or the Spat-product of the finite volume):

$$\begin{aligned} VOL &= x_\xi y_\eta z_\zeta + x_\eta y_\zeta z_\xi + x_\zeta y_\xi z_\eta \\ &- x_\xi y_\zeta z_\eta - x_\eta y_\zeta z_\xi - x_\eta y_\zeta z_\xi \end{aligned} \quad (2)$$

3.2 Artifical dissipation

Eq. 1 can be written in semidiscrete form:

$$\frac{\partial \vec{Q}}{\partial t} = -CO(\vec{Q}) + DN(\vec{Q}) + DA(\vec{Q}) + SO(\vec{Q}) \quad (3)$$

The convective fluxes are presented by the operator CO, the diffusive fluxes are described by the operator DN and the rotational sources build the operator SO. The artificial damping fluxes are added to the numerical scheme with the help of the operator DA containing both the second and fourth order damping.

$$DA(\vec{Q}) = D^2(\vec{Q}) - D^4(\vec{Q}) \quad (4)$$

with $D^2(\vec{Q}) = \partial(\Psi\epsilon_2(\nu(p))\partial\vec{Q})$
and $D^4(\vec{Q}) = \partial(\Psi\epsilon_4(\nu(p))\partial^3\vec{Q})$.
The scalar scaling factor Ψ is given by $\Psi = \Xi\lambda$, where Ξ is a scaled spectral radii and λ are the eigenvalues of the Jacobian matrices of the convective fluxes in the transformed frame. For more detail see [1] and [8]. The functions $\epsilon_2(\nu(p))$ and $\epsilon_4(\nu(p))$ are limiter of the second and fourth order damping operators with the static pressure as a sensor for shocks and stagnation points.

$$\epsilon_2(\nu(p)) = a_2 \max(\nu_{aroundcell})$$
$$\epsilon_4(\nu(p)) = \max(0, a_4 - \epsilon_2(\nu(p)))$$
$$a_2 = 0.45, \quad a_4 = 0.01$$

In the near of discontinuities $\epsilon_4(\nu(p))$ is blended and the damping is managed by $\epsilon_2(\nu(p))$. This leads the cell centred scheme to a quasi-upwind scheme of first order of accuracy. The sensor function ν is well known and given by

$$\nu(p) = \left| \frac{\partial^2 p}{p_{down} + 2p + p_{up}} \right|$$

3.3 Explicit Runge Kutta time stepping scheme

Eq. 3 is solved using an explicit scheme based on Runge-Kutta to gain stability. A five step scheme with $\alpha_i = (\frac{1}{4}, \frac{1}{6}, \frac{3}{8}, \frac{1}{2}, 1)$ allows CFL-numbers up to 3.5 in some cases. For steady calculations a local maximal time step calculated from the Courant-Friedrichs-Lewy criteria is used to gain convergence in a minimum number of Runge-Kutta iterations, with

$$\Delta t = \frac{\Delta t_{conv} \Delta t_{diff}}{\Delta t_{conv} + \Delta t_{diff}} \quad (5)$$

The convective time step is calculated from the sum of the transformed eigenvalues:

$$\Delta t_{conv} = (\lambda_\xi + \lambda_\eta + \lambda_\zeta)^{-1}$$

and the diffusive time step is yield from:

$$\Delta t_{diff} = \frac{(VOL)^2}{2.5\frac{\kappa\mu}{\rho Pr}(S_\eta^2 S_\zeta^2 + S_\xi^2 S_\zeta^2 + S_\zeta^2 S_\xi^2)}$$

and S the distances between neighbouring grid points. An implicit residual smoothing procedure introduced by Lerat ([7]) is used to extend the stability limit and the robustness of the Runge-Kutta scheme for steady state simulations. The smoothing procedure can be written in the following form:

$$(1 - b_\xi\partial_\xi^2)(1 - b_\eta\partial_\eta^2)(1 - b_\xi\partial_\zeta^2)RES_{new} = -RES_{old} \quad (6)$$

with the algorithm: $-\frac{\partial\vec{Q}}{\partial t} = RES_{old}$, smooth the residuals with Eq. 6 and build $\Delta\vec{Q} = RES_{new}\Delta t$.

3.4 Boundary conditions

All boundary conditions are specified in so called dummy or mirror cells. The prescribed code uses two layers of dummy cells at every block face. This ensures a full fourth order damping operator at every block interface.

3.4.1 In- and Outflow conditions

At inflow and outflow block faces characteristic variable boundary conditions described in [11] and with rotation in [5] are used. These conditions do not reflect incoming and outgoing waves. The 3D-Euler equations are transformed to their canonian form and local onedimensional flow is considered normal to the boundary. Due to the sign of the eigenvalues of the system we can descide between four possible flow situations at the block face where fluid should flow in or out:

1. Supersonic normal inflow:
   All eigenvalues have the same sign. All flow variables are specified from the farfield.

2. Subsonic normal inflow:
   Four eigenvalues have the same sign, one is differing. The following form can be derived from the characteristic variables:

$$p_{bound} = \frac{1}{2}[p_{extr} + p_{farf} \pm \rho c_0 \vec{\Gamma}(\vec{V_{extr}} - \vec{V_{farf}})] \quad (7)$$

   and the other primitive variables:

$$\begin{aligned} \rho_{bound} &= \rho_{extr} + \frac{p_{bound} - p_{extr}}{c_0^2} \\ \vec{V_{bound}} &= \vec{V_{extr}} \pm \vec{\Gamma} h \end{aligned} \quad (8)$$

   and $h = \frac{p_{extr} - p_{bound}}{\rho_0 c_0}$, $\vec{\Gamma} = (\Gamma_x, \Gamma_y, \Gamma_z)^T$

3. Supersonic normal Outflow:
   Again all eigenvalues have the same sign. All flow variables are extrapolated from the interior.

4. Subsonic normal Outflow:
   Four eigenvalues have the same sign, one differs. The primitive variables are calculated from:

$$\begin{aligned} p_{bound} &= p_\infty \\ \rho_{bound} &= \rho_{extr} + \frac{p_{bound} - p_{extr}}{c_0^2} \\ \vec{V_{bound}} &= \vec{V_{extr}} \pm \vec{\Gamma} h \end{aligned} \quad (9)$$

   and $h = \frac{p_{bound} - p_{extr}}{\rho_0 c_0}$.

3.4.2 Wall boundaries

The non-slip condition at body surfaces is used. No fluid passes a solid wall which is ensured using Eq. 10:

$$(\vec{V} - \vec{\omega} \times \vec{r})\vec{n} = 0, \quad \vec{V} = 0 \quad (10)$$

For diabatic walls a wall temperature or wall heat flux has to be specified as a wall boundary condition for the energy equation. The static pressure for the Navier-Stokes equations at walls is extrapolated from the interior using high order extrapolating schemes. The fluxes of the artificial disspation operators ∂Q and $\partial^3 Q$ should also vanish at walls to guarantee an impermeable surface.

3.4.3 Block interfaces, face of symmetry and periodicity

For accurate calculations block interface cells should feel like interior cells. Therefore the whole vector $\vec{Q}$ of the conservative variables is specified in every dummy cell layer of the regarding block. In the case of symmetry condition Eq. 11 should also be considered.

$$\rho V_{n_{b1}} = -\rho V_{n_{b2}}, \quad n = (x, y, z) \quad (11)$$

At periodic block faces the velocity vector should be rotated one (rotor/stator-) pitch (φ_p). In the case of rotation around the x-axis one yields:

$$\begin{pmatrix} u \\ v \\ w \end{pmatrix}_{p1} = \begin{pmatrix} 1 & 0 & 0 \\ 0 & \cos(\varphi_p) & \sin(\varphi_p) \\ 0 & -\sin(\varphi_p) & \cos(\varphi_p) \end{pmatrix} \begin{pmatrix} u \\ v \\ w \end{pmatrix}_{p2} \quad (12)$$

Block face $p1$ is periodic to block face $p2$.

3.5 Turbulence modelling

Complex threedimensional flow around sharp edges, through holes and in strong mixing regions is always turbulent. Turbine rotor or stator flow with film cooling ejection belongs to such classes of highly turbulent flow with strong turbulence production at walls and in free shear layers. Algebraic turbulence models are not able to simulate such flows, especially in the case of convection and diffusion of turbulent kinetic energy, i.e. through film cooling holes. Therefore a turbulence model considering the above turbulence phenomena should be used or if the computer power is sufficient and the Reynolds number is not too high a Large Eddy Simulation can be taken into account.
The code uses the two equation low Reynolds number $k - \epsilon$ model of Lam and Bremhorst [6] (Eq. 13) in viscous regions with $y^+ < 30$, else the standard $k - \epsilon$ model for high Reynolds flow with $f_1 = 1$, $f_2 = 1$ and $f_\mu = 1$ is used.

$$\frac{\partial \vec{Q}}{\partial t} + \frac{\partial \vec{F_j}}{\partial x_j} = \frac{\partial \vec{F_{v_j}}}{\partial x_j} + \vec{S_{source}} \quad (13)$$

with: $\vec{Q} = (\rho k, \rho\epsilon)^T$, $j = 1, 2, 3$
$\vec{F_j} = (\rho u_j k, \rho u_j \epsilon)^T$, $\vec{F_{v_j}} = ((\mu_l + \frac{\mu_t}{\sigma_k})\frac{\partial k}{\partial x_j}, (\mu_l + \frac{\mu_t}{\sigma_\epsilon})\frac{\partial \epsilon}{\partial x_j})^T$
$\vec{S_{source}} = (P_{prod} - \rho\epsilon, \quad c_{e1} f_1 \frac{\epsilon}{k} P_{prod} - c_{e2} f_2 \frac{\epsilon^2}{k})^T$
and the eddy viscosity:

$$\mu_t = c_\mu f_\mu \rho \frac{k^2}{\epsilon} \quad (14)$$

The constants $\sigma_k, \sigma_\epsilon, c_{e1}, c_{e2}$ and c_μ are the standard coefficients.
Due to the source-dominant character of both equations the use of the same discretization scheme as for Eq. 1 and the same timestep may lead to a non stable scheme. The prescribed codes uses an explicit or implicit time discretization and a first order upwind spatial discretization (Eq. 15) for the convective fluxes of k and ϵ. The diffusive terms are discretized using the cell centred second order discretization as described before. The flux Φ through surface $S_{i+1,j,k}$ and surface $S_{i,j,k}$ is calculated from:

$$\begin{aligned} \Phi_{i+1,j,k} &= \max[\dot{m}_{i+1,j,k}, 0]\varphi_{i,j,k} - \\ &\quad \max[-\dot{m}_{i+1,j,k}, 0]\varphi_{i+1,j,k} \\ \Phi_{i,j,k} &= \max[\dot{m}_{i,j,k}, 0]\varphi_{i-1,j,k} - \\ &\quad \max[-\dot{m}_{i,j,k}, 0]\varphi_{i,j,k} \end{aligned} \quad (15)$$

with $\varphi = (k, \epsilon)^T$ and $\dot{m}$ representing the transformed massflow through the cell faces.
Stability in the explicit formulation is gained using sub-iterations per time step with a somewhat smaller timestep.
The implicit formulation uses a SOR scheme with ν Newton iterations and 2ν Gauss-Seidel overelaxation sweeps with a relaxation factor of 1.2 per time step.

The implicit non-factorized formulation of Eq. 13 leads to Eq. 16:

$$VOL\frac{\Delta q^{\nu+1}}{\Delta t} + A^{\nu} + B^{\nu} + C^{\nu} = VOL\frac{Q^{n} - q^{\nu}}{\Delta t} + S^{\nu} - RHS \quad (16)$$
$$RHS = S^{n} - F_1^{n} - F_2^{n} - F_3^{n}$$
$$q^{\nu+1} = q^{\nu} + \Delta q^{\nu+1}$$

The matrices $A^{\nu}, B^{\nu}, C^{\nu}, S^{\nu}$ are the Jacobian of the fluxes and the source term.

4 Multi-blocking and data administration

The code works on structured grids in unstructured multi-block manner. There are no limits concerning the number of blocks and piecewise specification of boundary conditions per block face. No recompilation is necessary when altering the boundary conditions and blocking of the flow problem.
All block data (conservative variables and metric) is located in the computer memory (IN-CORE) all the time, therefore no IO is necessary during a calculation. Nevertheless the computer-storage requirement is only 320 Words per mesh cell for a typical simulation. This can be reduced by massive blocking of the computational mesh.
Due to the accuracy and stability of the scheme data exchange between block interfaces is carried out at every Runge-Kutta step, which leads to a drop in the overall code-speed efficiency for massive blocking. All flow variables and metric quantities are stored in 1D-arrays allowing big loop sizes for the vectorization.
All calculations shown in section 5 were carried out on a NEC-SX3-1 with a peak performance of approximately 6.4GFlops. The simulation of the film cooling flow out of a single hole (10 blocks, 1.6 10^6 cells) achieved 1.5GFlops. Furthermore the code is parallized running on CM5 from "Thinking Machines" using message passing. No performance analysis was carried out until now. For more details about the code see [9], [3] and [10].

5 Applications and discussions

The described flow solver is validated and tested using two different film cooling test cases.

Test case 1 (see Fig. 1) deals with film cooling through slots near the leading edge of a turbine blade in a 2D-cascade. At mid span the flow is nearly twodimensional but looking at Fig. 2 the ejection slots are interrupted at two radial locations. The global blowing rate M_{bl} was 0.5. The experiments were carried out at the University of the Armed Forces in Munich ([2]).
The flow field was detaily measured using the L2F-technique [1] allowing measurements very close to walls. Furthermore oil flow pictures of the blade surfaces give some information about the developement of the threedimensional cooling film and the resulting secondary flow. Fig. 3 shows the computational mesh in the leading edge region of the blade consisting of one C-type mesh around the blade and five H-type meshes around. The whole 3D mesh consists of 561000 cells. Due to the strong flow gradients at the stagnation point and the expected deformation of the ejection profiles of the film the cooling slots and internal blade cooling chamber has to be detected on the given mesh.

Fig. 4 presents the comparison between measured and calculated data for the velocity vector field and Fig. 5 for the amount of the velocity. The agreement is remarkable good especially looking at the size and location of the seperation bubbles. Due to the ejection in the stagnation region of the turbine blade the location of the designed profile stagnation point moves a little bit towards the suction side. Therefore the pressure side slot feels a somewhat lower pressure than the suction side slot. This fact leads to a higher blowing rate at the pressure side and as a result the cooling film seperates from the surface. At the pressure side only a small seperation zone is found downstream of the slot. Due to the strong deformation of the ejected cooling flow and the interaction with the upstream outer flow a small seperation bubble is found inside the pressure side slot. The experiment showed an oil deposit at the same location confirming the calculation.
Fig. 6 presents the experimental oilflow picture of one particular part of the blade pressure side. In comparison the calculated flow field is given in Fig. 7. Due to the broken cooling slots a 3D flow field develops in the mixing region of the cooling film and the main turbine flow. The flow is accelerated through the slot interuptions, feels the low pressure area at the lee-side of the cooling slot and recirculates below the large seperation bubble shown in Fig.4 and 5. In real gas turbines this flow situation will lead to destruction of the blade as a result from overheating. Again the comparison between measured and calculated data is good.

Test case 2 deals with cooling air ejection from a row of holes with an ejection angle of 30° and a hole to pitch ratio of about 2.5. The investigated blowing rate was approximately 2.0. Fig. 8 shows the blade of the highly loaded turbine and the location of the film cooling holes. Again the measurements were carried out at the University of the Armed Forces in Munich ([12], [13]). The technique of the 3D subminiature

[1] Laser 2 Focus technique

hot wire probe was applied to measure the complex 3D flow field.

The computational domain is shown in Fig. 8. Due to the complexibility of the problem only a part of the whole flow field is calculated and boundary conditions are obtained from a calculation for one pitch of the cascade. The Reynolds No. of the cascade flow based on the axial chord length is 500000, the Reynolds No. of the model problem in the reduced domain based on the blowing-hole diameter is 6000. Due to this low Reynolds No. and the capability of the prescribed DLR computer a future step should be a LES [2] on a fine mesh.

The computational mesh consists of 10 blocks with a least 220000 cells on the coarse mesh and 1600000 cells on the fine mesh. Fig. 9 presents the mesh in two sights. Due to the symmetry line in the center of the hole only one half of the domain has to be calculated. The influence of the end walls of the cascade can be neglected when calculating a hole at mid span.

The following boundary conditions are used at inlet and oulet block faces:

Global blowing rate: $M_{blow} = 2.0$:

Outer turbine flow	
Tt_{in}	313 K
Pt_{in}	15230 Pa
Flow angles	surface fitted flow
Laminar boundary layer	core-flow: Tu=2.8 %

Cooling channel flow	
Tt_{in}	313 K
Pt_{in}	18700 Pa
Flow angles	surface fitted flow
Turbulent flow	core-flow: Tu=2.8 %

At the outlet of the computational domain a static pressure is prescribed.

The **measured** cooling mass flow rate was $23.3\frac{g}{s}$ for the whole cascade and 34 holes per row. The **calculated** mass flow rate was $23.21\frac{g}{s}$.

Detailed investigations of the mechanism of cooling air injection from a row of holes at turbine blade surfaces should give information about the mixing of the cooling flow and the primary flow, loss production and at least the cooling effect and protection of the turbine blade surface. The measurements show the influence of the developement of several vortex systems on the mixing and cooling of the film. Due to the change of the flow direction in the blowing hole (Fig. 10) the well known kidney vortex is generated. This vortex combines with a second vortex pair at the blowing hole exit. We will call this vortex chimney vortex because it is also visible at smoking chimneys with strong wind. The generation of this vortex is easy to declare. The outgoing cooling jet generates a strong free shear layer immediately downstream of the blowing hole exit. Looking at Fig. 11d one can recognize the starting point of the roll up of this chimney vortex. The shear layer is rubbed on, cooling flow breaks through this layer and rolls up due to the pressure gradient. This vortex rotates in the same direction as the kidney vortex and combines to a big vortex pair dominating the mixing with the primary flow. The kidney vortex is clearly visible looking at Fig. 11a and b. A very high eddy viscosity and turbulence intensity is generated at the sharp edge of the blowing hole entrance (Fig. 10a,b). The kidney vortex transportes this highly turbulent material through the blowing hole in the outer turbine flow. Fig. 11a,b shows the distribution of the turbulence intensity at a cross flow plane located at $\frac{x}{D_b} = 0$ in the center of the exit plane of the blowing hole. Compared with the primary flow which was laminar upstream from the cooling air ejection the turbulence intensity of the cooling jet is approximately 20 times higher. Furthermore the well known horse shoe vortex is generated immediately in front of the cooling jet. The size of this vortex depends on the upstream boundary layer. A laminar boundary layer favours the developement of the horse shoe vortex. Looking in downstream direction this vortex rotates counterclockwise on the right hand side of the blowing hole and clockwise on the left hand side. The track of the horse shoe vortex around the blowing hole is clearly to be seen in Fig. 15. In the calculation this vortex diffuses very quickly. The experiment may locate the horse shoe vortex riding on the jet but diffusing also very quickly. For the mixing mechanism this vortex does not matter any way.

The crossflow planes located at $\frac{x}{D_b} = 1$, $\frac{x}{D_b} = 5$ and $\frac{x}{D_b} = 10$ are compared with experimental data (s. Fig. 8). The data of the velocity field, turbulence level and the x-component of the vorticity are compared. It should be mentioned that the line of sight is in downstream direction in the experiment and in upstream direction in the calculation. Furthermore it should be mentioned that a certain part of the flow close to the wall could not be measured due to the size of the hot wire probe and the interaction with the wall. The blended region is found below the straight line in Fig. 12-13.

Fig. 10 presents a side view of the blowing area. As mentioned earlier the mechanism of turbulence production is well documented by these figures. A lot of turbulence is produced at the sharp edge at the entrance of the coolent in the blowing hole in the cooling channel. Furthermore the strong shear layer at the blowing hole exit on the upstream side produces a strong turbulent flow. Due to the mixing with the main flow turbulence diffuses downstream. The incoming upstream boundary layer of the main flow is clearly visible. The thickness is $\delta \approx 1/2 - 1D_b$. The

[2] Large Eddy Simulation

upstream boundary layer is laminar and becomes turbulent at the blowing location.

Fig. 11 shows the first cross flow plane located at $x/D_b = 0$ in the center of the exit of the hole. No experimental data is available at this location. The kidney shaped vortex coming out of the blowing hole is visible looking at the toatal pressure ratio or the turbulence intensity. The turbulent kinetic energy is very high in the center of the hole and of course very high close to the hole walls. The velocity field is only plotted for the right part of the outgoing jet demonstrating the mixing with the outer flow and the production of the chimney vortex as discussed before. The vorticity distribution shows the kidney vortex and the strong rotation in the shear layer of the jet.

Fig. 12 presents the data at the cross flow section $x/D_b = 1$. In comparison the expermental data is shown in Fig. 16. The measured turbulence level related to the absolute velocity presented in Fig. 16 shows a slight asymmetry which should not appear. Compared with the calculated data one can state that both data is in the same range. The flow field of experimental and calculated data show the strong burst of the jet and the developement of the combined kidney and chimney vortex. The vortex center is close to the wall and blended in the experimental data. The effect is visible in the oil-flow picture in Fig. 19. The distribution of the vorticity show the developement of the chimney vortex. The comparison with the experimental data show good agreement. The size of the upper peak is calculated too small. The total pressure ratio gives some information about the location of the shear layer (under the jet) and areas with high pressure coming out of the hole. Furthermore the jet-burst and the break through of coolant at the 'west and east' side of the jet is visible in the total pressure distribution.

The cross flow plane at $x/D_b = 5$ is represented in Fig. 13 and Fig 17. The comparison of the calculated and measured distribution of the turbulence level is remarkable good. The jet sucks material with high turbulent energy from the turbine surface boundary layer into its center and looks like an atomic mushroom cloud. This secondary jet normal to the surface splits the coolant jet into two parts. Again this secondary jet and streamlines are visible in Fig. 19 and Fig. 15. The calculated and measured velocity field supports the impression of the split of the jet. The combined kidney and chimney vortex is the main driving force for the secondary jet. The total pressure distribution represents two areas at both sides of the coolant jet with high pressure and low pressure areas in the center. Even the calculated distribution of the vorticity compared with the measured data is good.

Fig. 14 and Fig. 18 show data for the cross flow plane at $x/D_b = 10$. Again the comparison between measured and calculated turbulence level and vorticity distribution show good agreement. The peak turbulence intensity compared with the other cross flow planes is lower, the jet is bursting, mixing and lifting more and more. The velocity field demonstrates the large vortex system and the entrainment of material in the jet.

The comparison between measured and calculated data shown for the cross flow planes should be carried out regarding the blended near-wall region in the experiment.

6 Summary

The mechanism of cooling fluid ejection to protect turbine blade surfaces is theoretically investigated by solving the Reynolds-averaged Navier-Stokes equations using a Finite volume solver working on patched structured grids in unstructured multi block manner to yield a maximal flexibility concerning vectorization, parallelization and geometry discretization.

Two different calculations with film cooling are carried out and compared with experimental data. The first calculation deals with film cooling in the leading edge region of a turbine blade. Coolant is ejected through slots. The interaction between the primary flow and the cooling film is simulated very accurately. The second calculation deals with film cooling from a single row of holes at the suction side surface of a highly loaded turbine blade. The mechanism of mixing and vortex generation and diffusion is investigated numerically and compared with experimental data. The strong influence of the shape of the cooling channel and blowing hole geometry on turbulence and vortex generation is shown. The comparison with measured data, even for turbulence levels shows the efficiency of the Navier-Stokes solver. With the help of these tools it should be possible to investigate the influence of several film cooling parameters on the cooling effect in detail. In the author's opinion it should be possible to influence the direction of the rotation of the kidney vortex by changing the geometry and configuration of the internal cooling system. The kidney vortex system and the chimney vortex may remove each other improving the efficiency of film cooling and saving cooling air.

Using better turbulence models to account for the nonisotropic character of turbulence in complex 3D flows (2nd moment closure) or trying out LES in future will improve the accuracy of the theoretical data.

References

[1] Arnone, A.: *'Viscous Analysis of Three-Dimensional Rotor Flows Using a Multigrid Method'*, NASA Tech. Memorandum 106266, ICOMP-93-25 (1993)

[2] Beeck, A.: *'Strömungsfelduntersuchungen zum areodyamischen Verhalten eines hochbelasteten Turbinengitters mit Kühlluftausblasung an der Vorderkante'* Dissertation Bw-Hochschule in München (1992)

[3] Heselhaus, A.; Vogel, D.T. and Krain, H.: *'Coupling of 3D-Navier-Stokes External Flow Calculations and Internal 3D-Heat Conduction Calculations for Cooled Turbine Blades'*, AGARD-paper 41 (1992)

[4] Holmes, D.G. and Tong, S.S.: *'A Three Dimensional Euler Solver for Turbomachinery Blade Rows'* ASME, April (1985)

[5] Kroll, N.: *'Berechnung von Strömunsfeldern um Propeller und Rotoren im Schwebeflug durch die Lösung der Euler-Gleichungen'* DLR-FB 89-37 (1989)

[6] Lam, C.G. and Bremhorst, K.A.: *' Modified Form of the k-ϵ model for prediction wall turbulence'*, J. of Fluid Eng. 103, pp 456-460 (1981)

[7] Lerat, A.: *'Une class de Schemas aux Differences Implicites Pour les Sytemes Hyperboliques de Lois de Conservation'* Comptes Rendus Acad. Sciences, Paris, Vol 288 A (1979)

[8] Swanson, R.C. and Turkel, E.: *'Artificial Dissipation and Central Difference Schemes for the Euler and Navier-Stokes Equations'* AIAA paper 87-1107 (1987)

[9] Vogel, D.T.: *'Computation of 3D-viscous flow and heat transfer for the application to film cooled gas turbine blades'*, AGARD-paper 7 (1991)

[10] Vogel, D.T.: *'Navier-Stokes Calculation of Turbine Flows with Heat Transfer and Film Cooling*, Int. Symposium 'Gas Turbines and Gas Cycle Plants', Bled Slovenia, (1993)

[11] Whitfield, D.L.: *'Three-Dimensional Unsteady Euler Equation Solutions Using Flux Vector Splitting'* NASA-CR-173254 (1983)

[12] Wilfert, G.: *'Mischungsvorgänge zwischen Kühlfilmen und Grenzschichten fortschrittlicher Turbinenbeschaufelungen'* FVV-Zwischenbericht, Forschungsprogramm: Aerodynamik der Filmkühlung. (1993)

[13] Wilfert, G. and Fottner, L.: *'The Aerordynmaic Effect of Discrete Cooling Jets with the Mainstream Flow on a Highly Loaded Turbine Blade'* ASME paper 94-GT-235, Netherlands (1994)

7 Figures

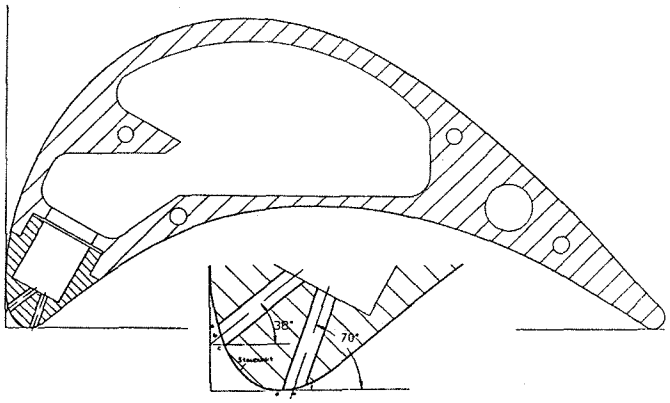

Figure 1: Turbine blade with slot ejection at leading edge

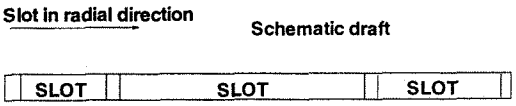

Figure 2: Slot in radial direction

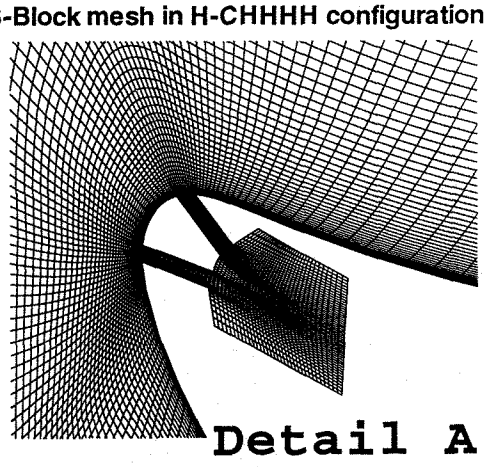

Figure 3: Ejection region with three inner "H"-meshes and outer "C"-mesh.

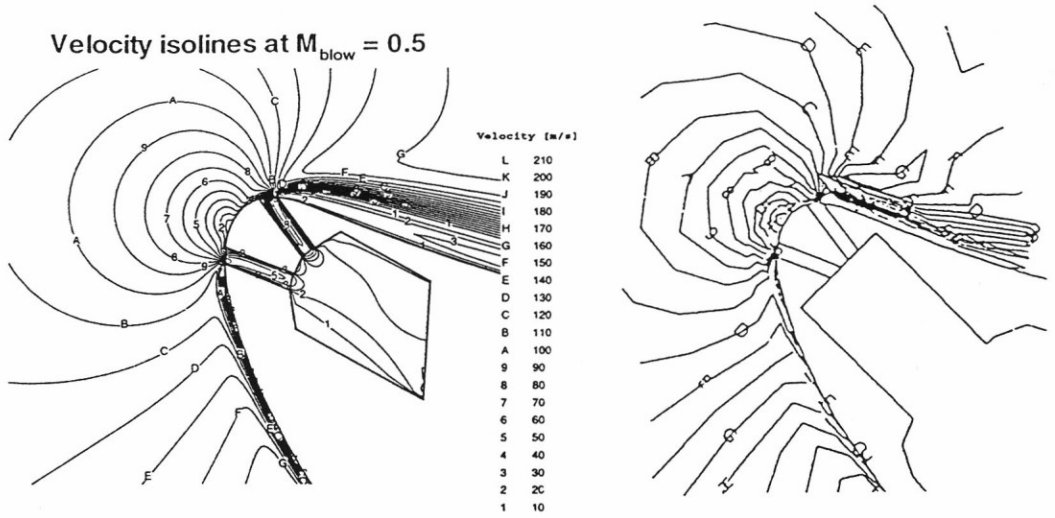

Figure 4: Velocity isolines, left side: **calculated**, right side: **measured**

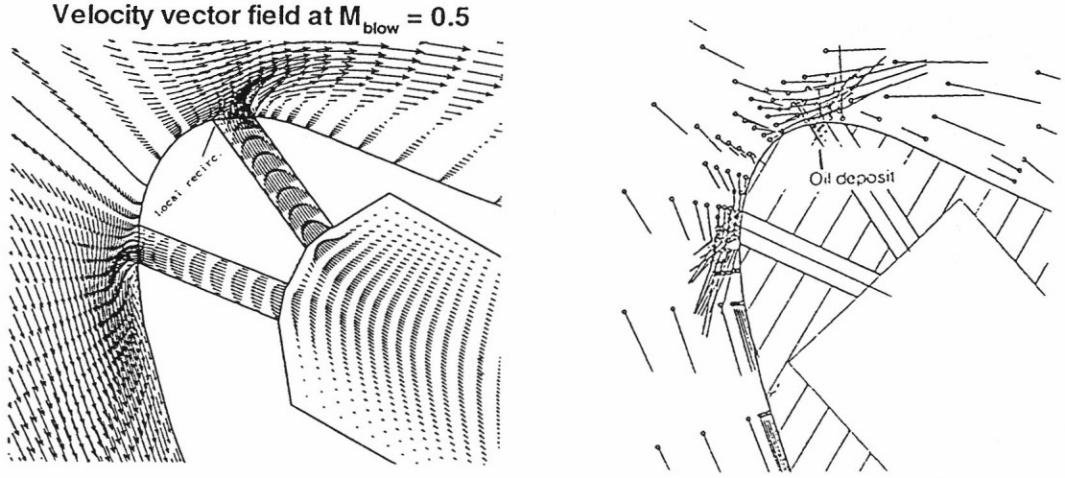

Figure 5: Velocity vectors, left side: **calculated**, right side: **measured**

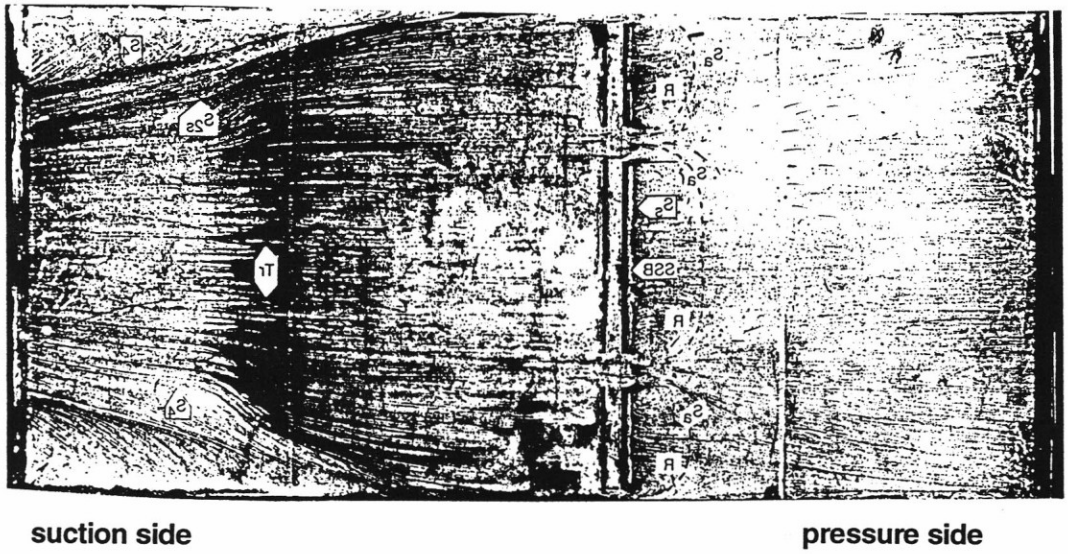

Figure 6: Oilflow on the turbine blade pressure side (measured)

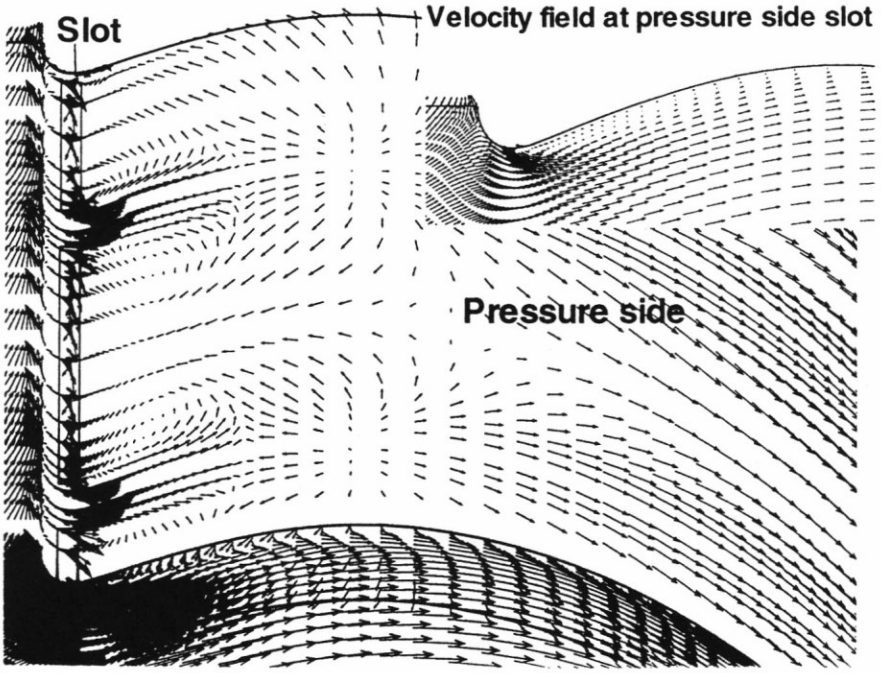

Figure 7: Oilflow on the turbine blade pressure side (calculated)

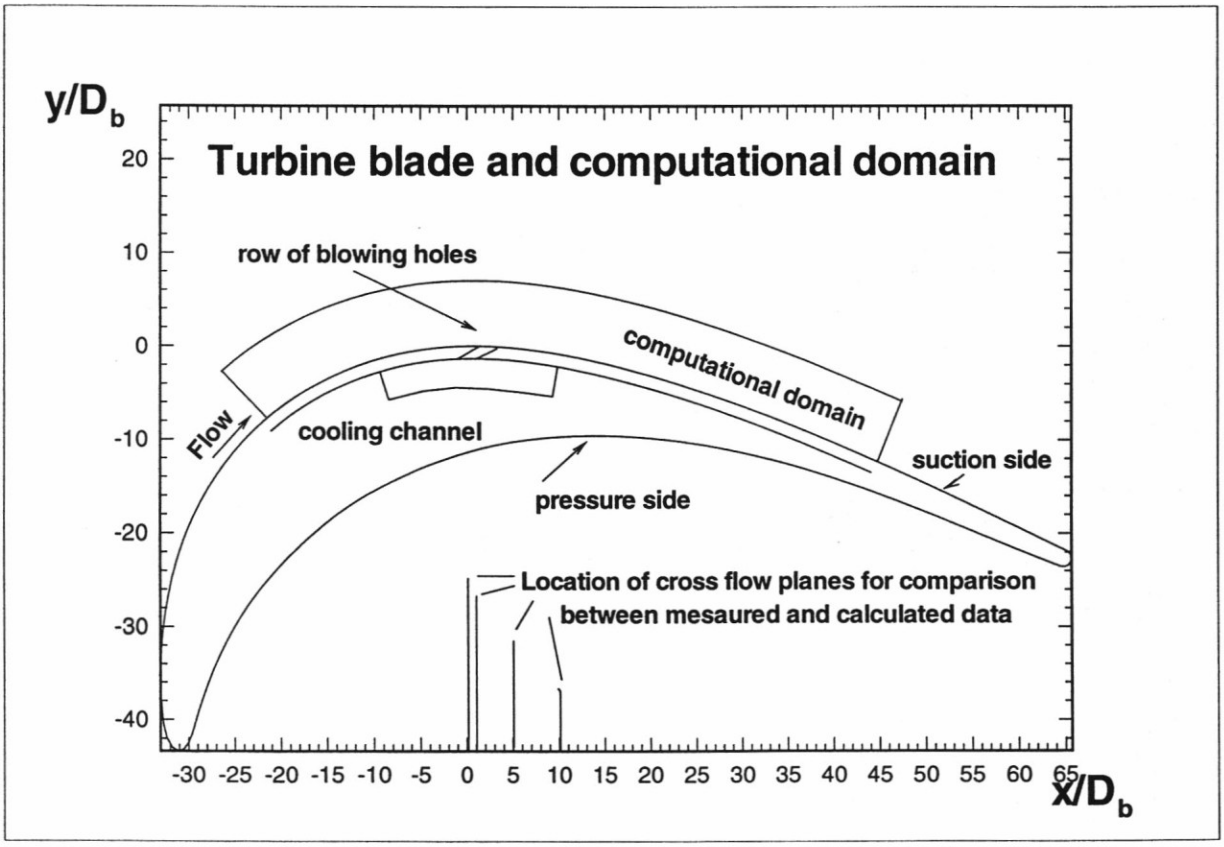

Figure 8: Computational domain

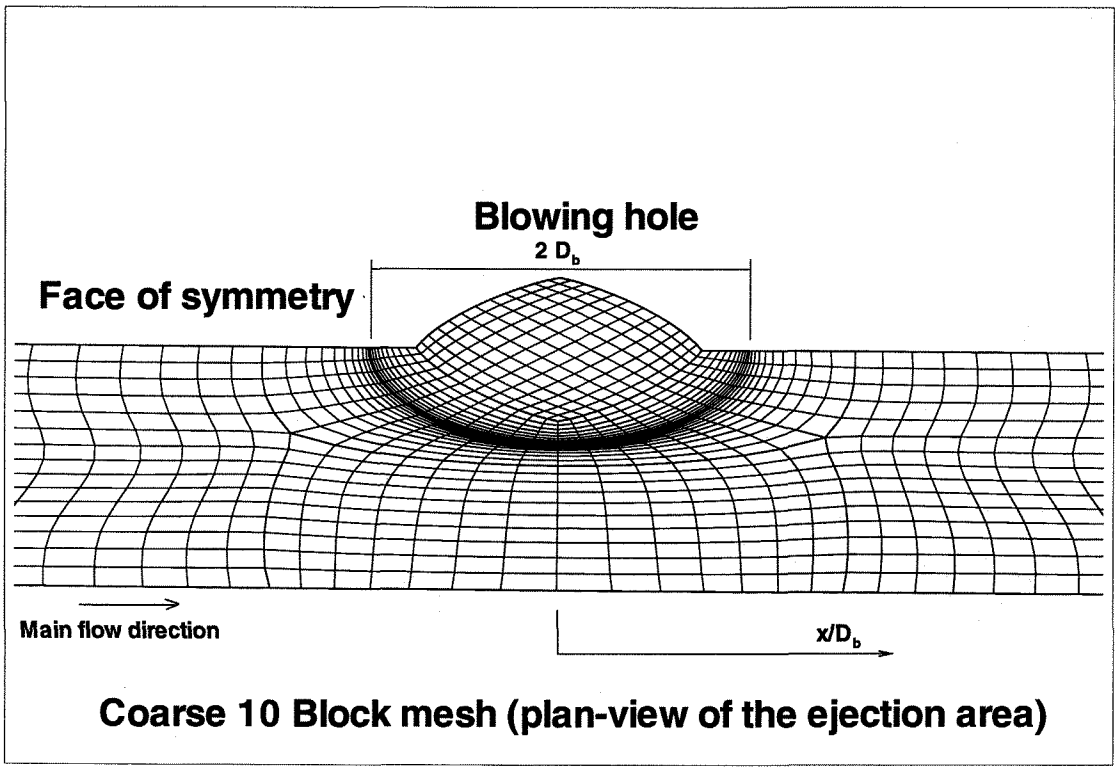

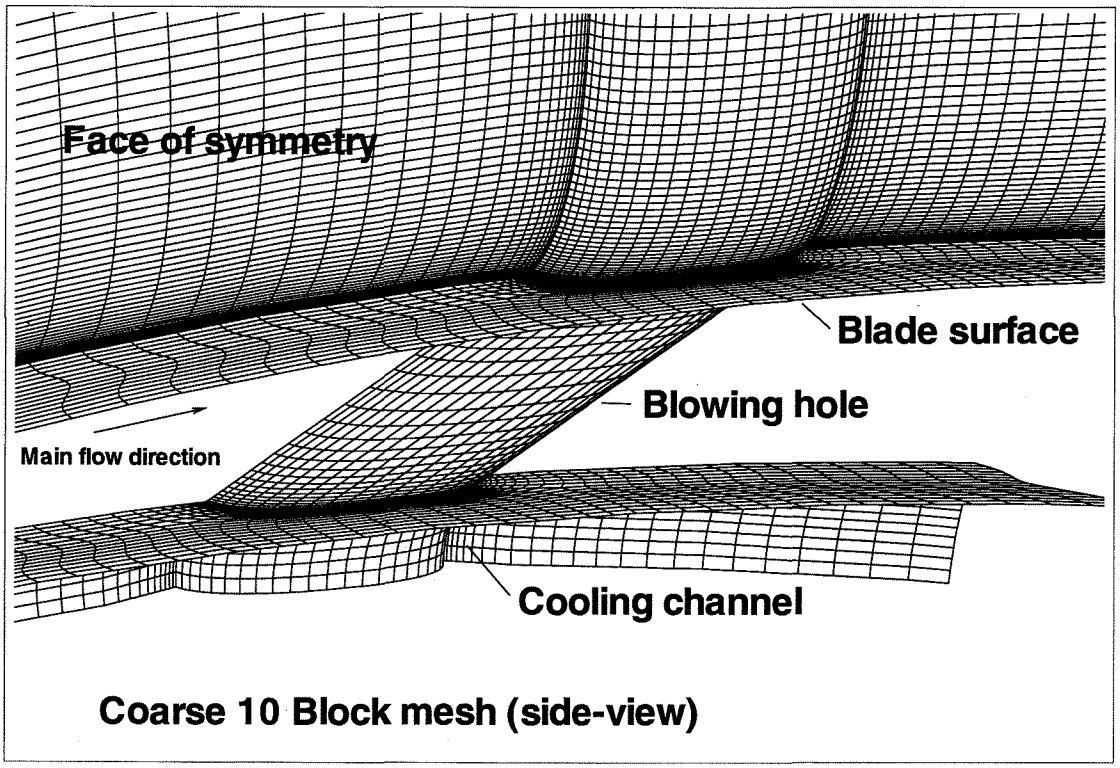

Figure 9: Computional mesh in plan and side view

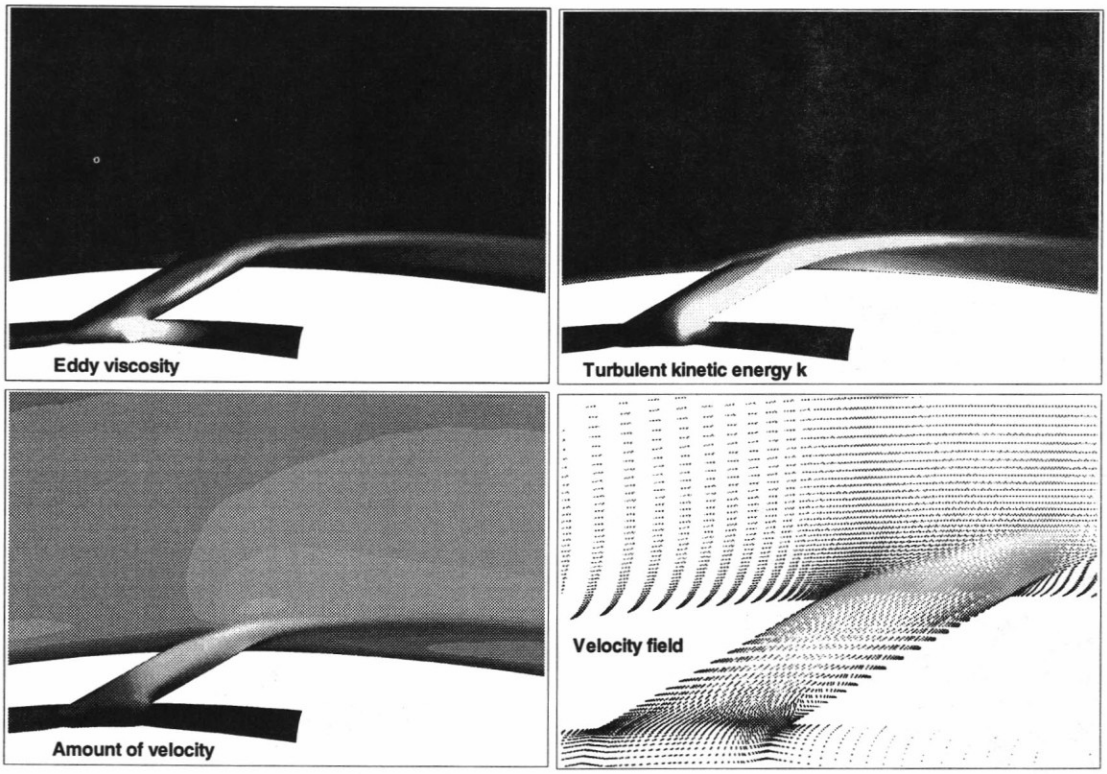

Figure 10: Calculated data from side view (center of hole)

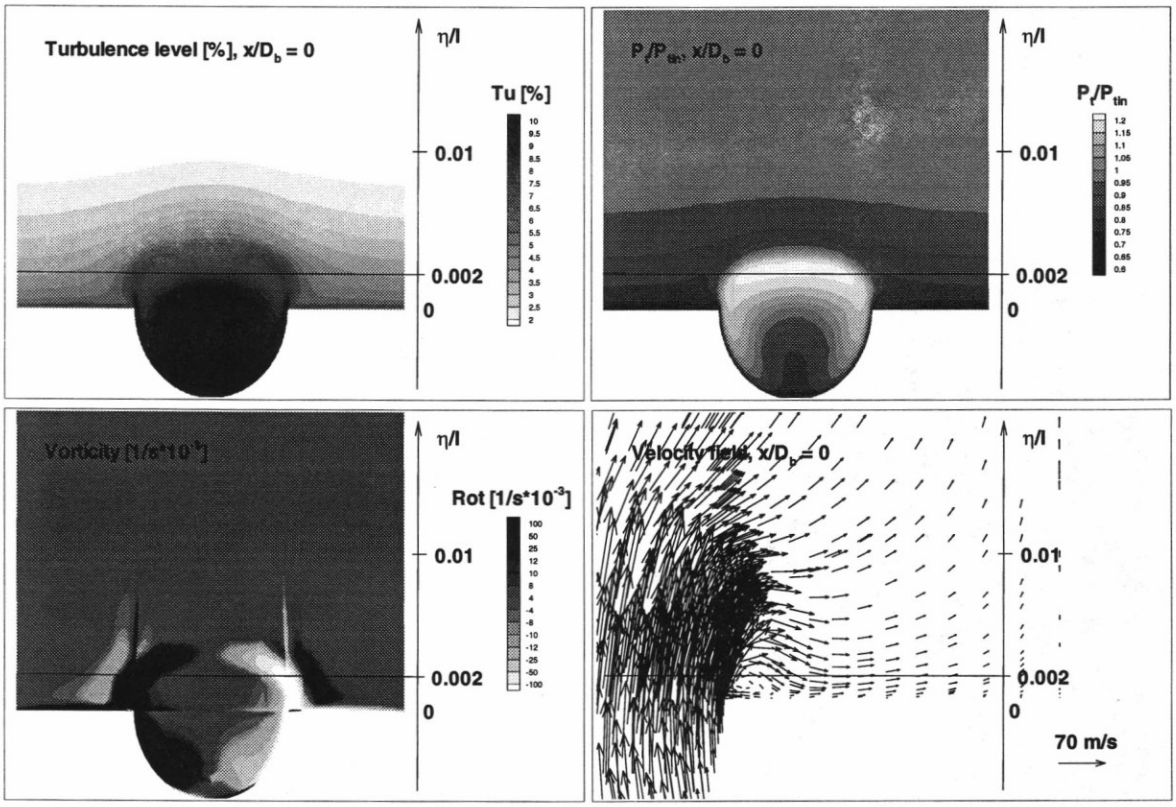

Figure 11: Calculated data at cross flow section $x/D_b = 0$

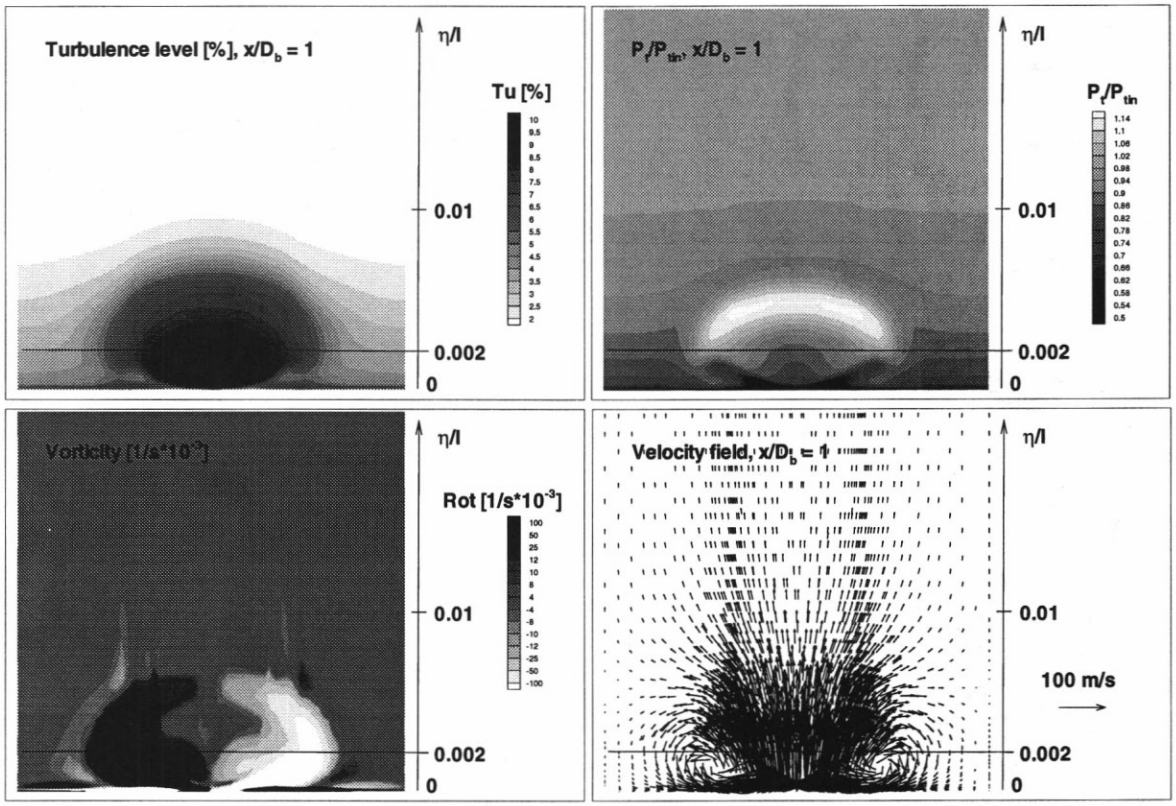

Figure 12: Calculated data at cross flow section $x/D_b = 1$

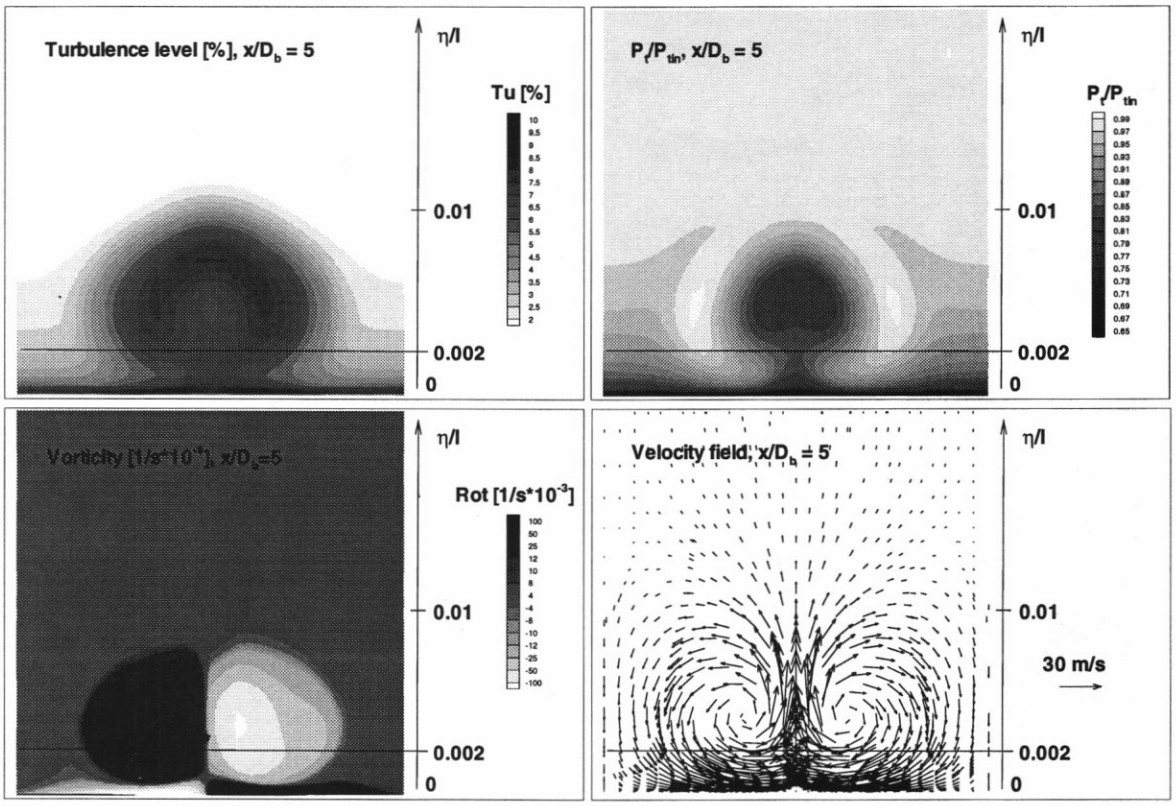

Figure 13: Calculated data at cross flow section $x/D_b = 5$

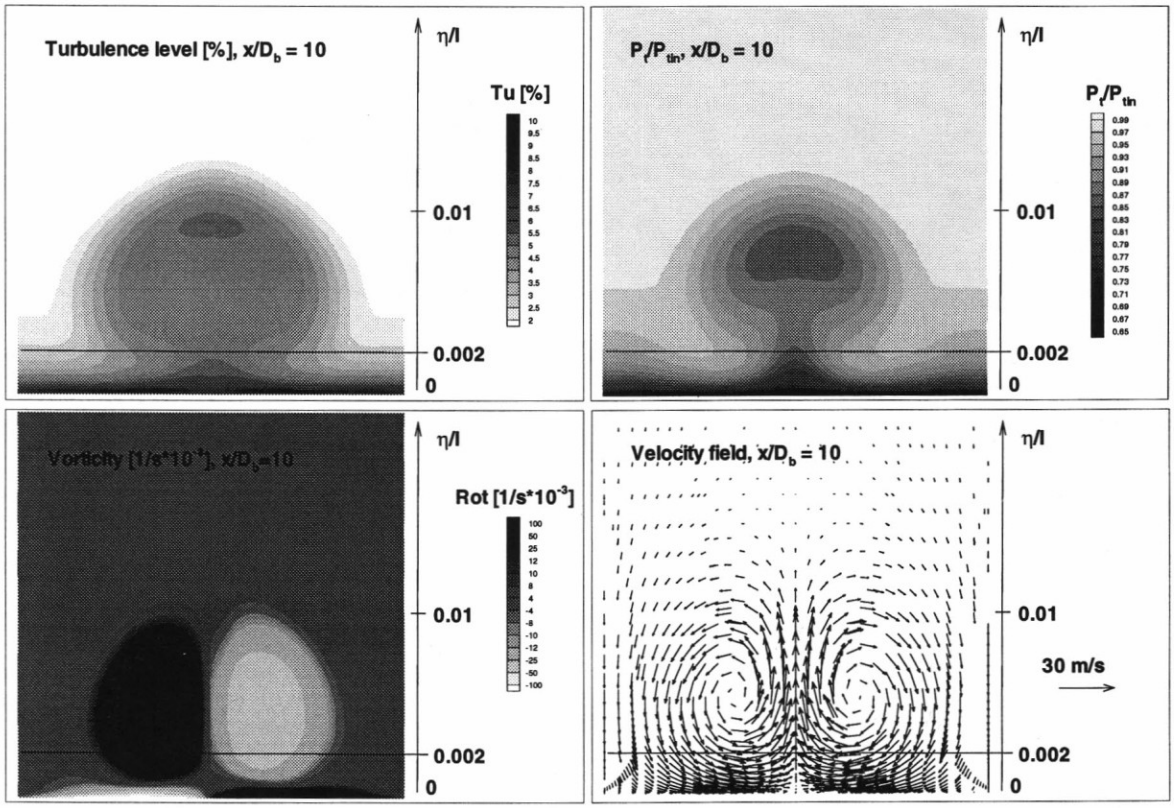

Figure 14: Calculated data at cross flow section $x/D_b = 10$

$M_{blow} = 2.0$

Surface oil-flow streamlines

Outer turbine surface

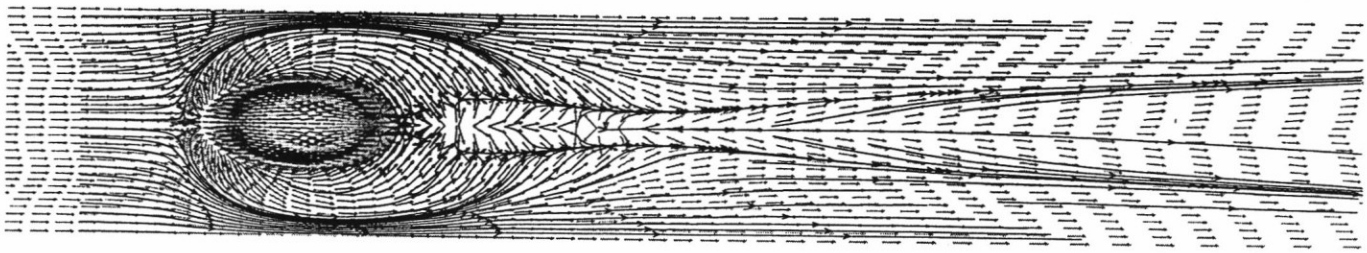

Figure 15: Oilflow on the turbine blade suction side (calculated)

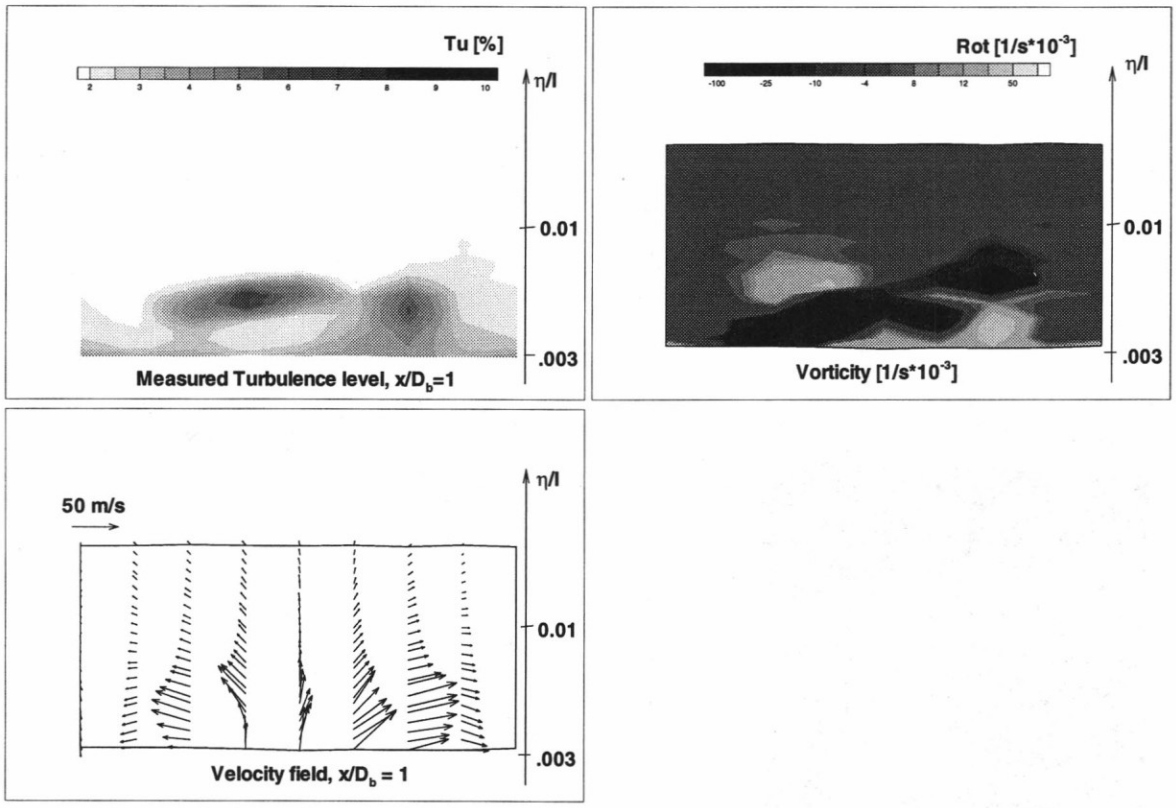

Figure 16: Measured data at cross flow section $x/D_b = 1$

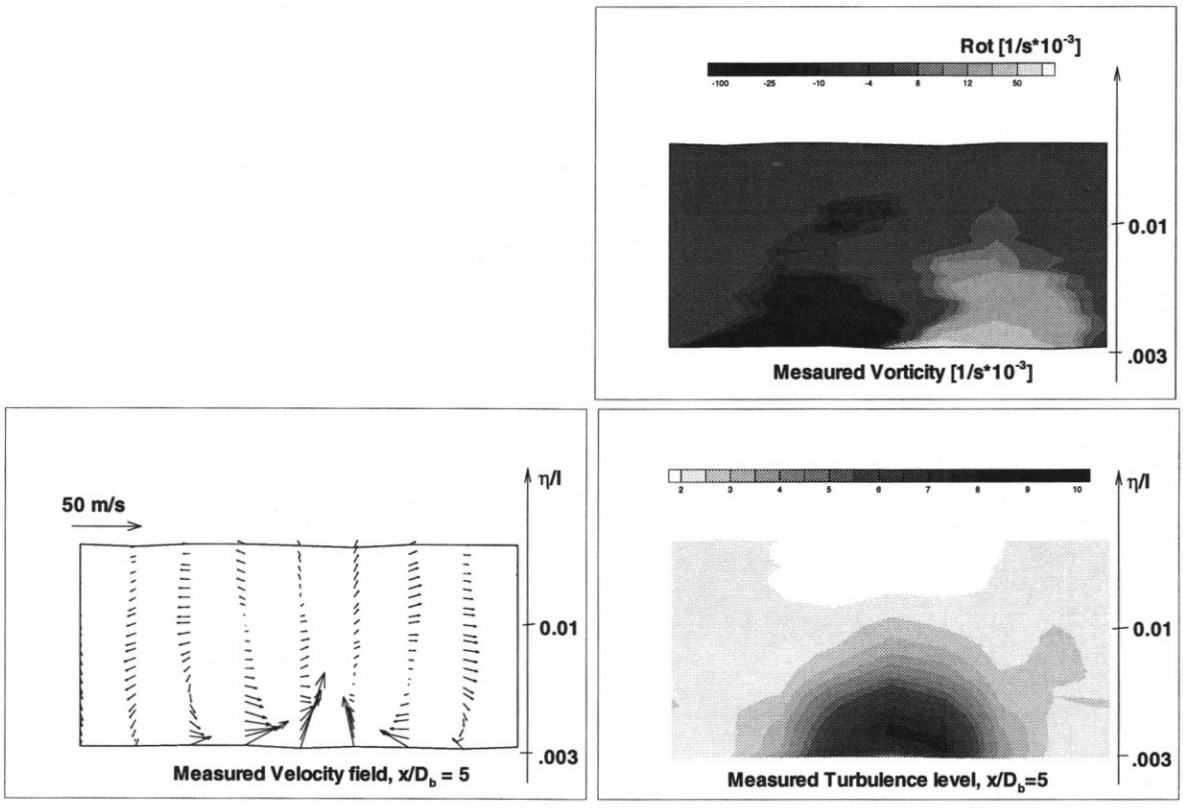

Figure 17: Measured data at cross flow section $x/D_b = 5$

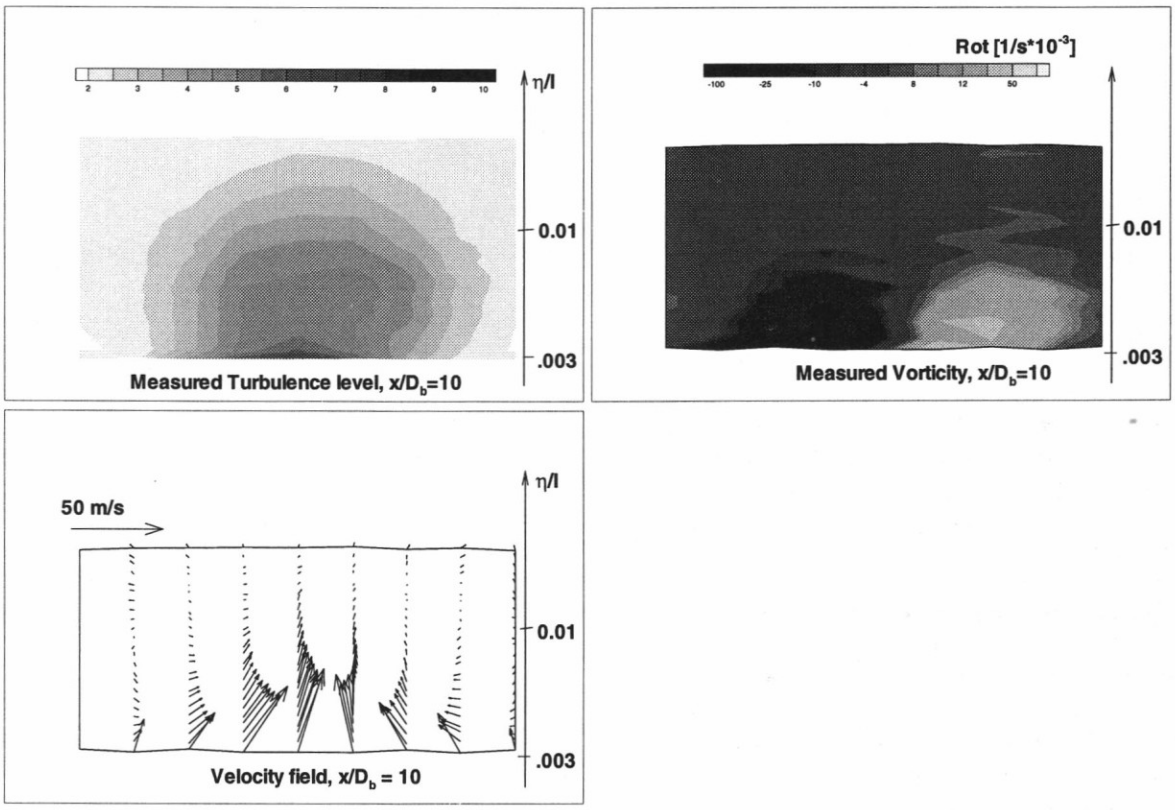

Figure 18: Measured data at cross flow section $x/D_b = 10$

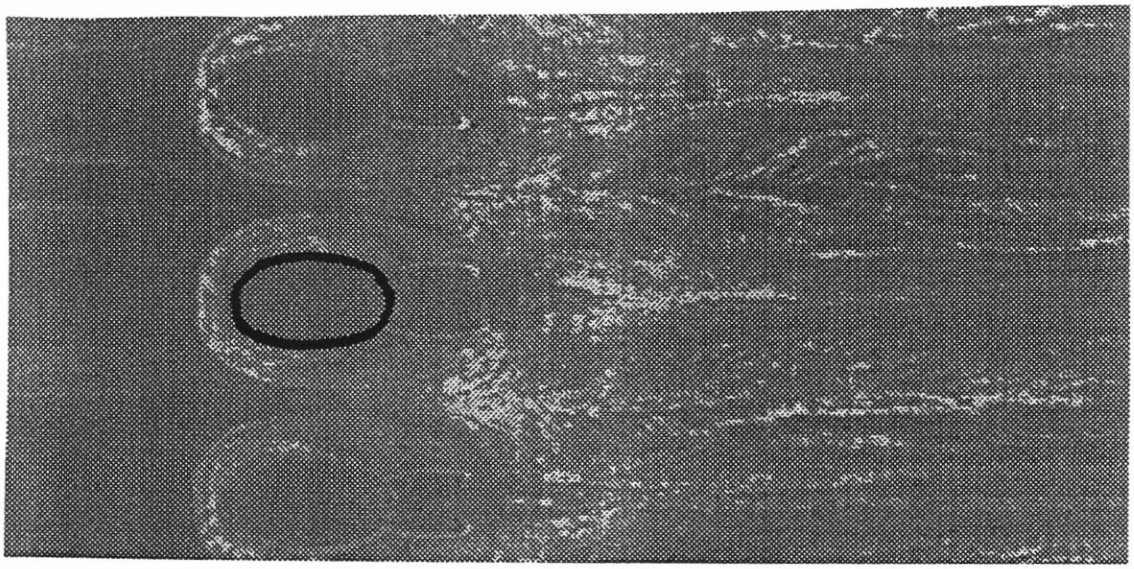

Figure 19: Oilflow on the turbine blade suction side (measured)